Original Article

Reversible α′ ↔ β′ transformation in a textured Sm-sialon ceramic

Andrew Carman [a,*], Elena Pereloma [a], Yi-Bing Cheng [b]

[a] School of Mechanical, Materials and Mechatronics Engineering, University of Wollongong, NSW 2522, Australia
[b] Department of Materials Engineering, Monash University, VIC 3800, Australia

Abstract

A preferential orientation was observed in a Sm-sialon ceramic, of the composition $Sm_{0.4}Si_{9.6}Al_{2.4}O_{1.2}N_{14.8}$, after hot pressing at 1800 °C for 2 h. Post-sintering heat treatment was performed at 1450 °C for 384 h, resulting in the forward α′ → β′ transformation, accompanied by the formation of M'_{SS} and an increase in the 21R phase. Subsequent heat treatment at 1800 °C for 2 h resulted in the reverse β′ → α′ transformation, with a corresponding decrease in the M'_{SS} and 21R phases. This confirms the fully reversible reaction of α′ + liquid ↔ β′ + M'_{SS} + 21R in Sm-sialon ceramics. In addition, the texture introduced by hot pressing was maintained after all heat treatments, indicating that there is a crystallographic relationship between the transformation phases. The microstructure and mechanical properties were also found to be mostly reversible, contrary to the behaviour of the α′ lattice parameters and bulk density.
© 2010 Elsevier Ltd. All rights reserved.

Keywords: Sialon; Hot pressing; Microstructure-final; Mechanical properties; Transformation cycling

1. Introduction

The α′ → β′ transformation in sialon ceramics poses a hurdle to their use in industrial applications, as the application temperatures for which sialons are designed fall within the transformation temperature ranges for most sialon compositions. However, the reversibility of the α′ ↔ β′ transformation suggests the ability to reverse any degradation or change in properties that may result from the α′ → β′ transformation by simply re-heating the component to higher temperatures. Despite this possibility, there have been very few studies of the reverse transformation route.[1–3] While the forward α′ → β′ transformation has been extensively studied in terms of sialon composition and stabilising cation(s) added,[4–6] heat treatment temperature and time[6–8] and amount and composition of glass/liquid phase,[5,8] the reverse β′ → α′ transformation has attracted little attention. The few studies that have investigated the reverse β′→ transformation have tended to only demonstrate its existence and report on its effects on physical and mechanical properties. The effects on, and involvement of, secondary phases has only been studied in the Nd–Si–Al–O–N system,[3] which is less appropriate for industrial applications due to the inherent thermal instability of the Nd-α-sialon phase.

A possible advantage of the reversible α′ ↔ β′ transformation is in sialon design and processing for ceramic components. The forward and reverse transformation routes may provide an excellent manufacturing opportunity to tailor and produce a number of sialon ceramic components from a single composition. This would eliminate, or at least minimise, the compositional design stage of sialon fabrication, which is very sensitive to a number of factors.

Therefore, it is important to develop our understanding of the reversibility of the α′ ↔ β′ transformation. The reversibility of the α′ ↔ β′ transformation has been clearly established for Nd-sialons, as well as its effects on the microstructure and properties of the material.[3] However, the behaviour of the α′ → β′ transformation can be dramatically affected by the composition of the sialon. Therefore, the reversibility of the α′ ↔ β′ transformation needs to be established in different sialon compositions in order for it to be more thoroughly understood. In the current study, a Sm-sialon composition was subjected to a cycle of the α′ ↔ β′ transformation and its effects on the texture, microstructure, and physical and mechanical properties were investigated.

* Corresponding author at: School of Mechanical, Materials and Mechatronics Engineering, University of Wollongong, Building 2, Room 104, St Pauls, NSW 2522, Australia. Tel.: +61 2 4221 5904; fax: +61 2 4221 3662.

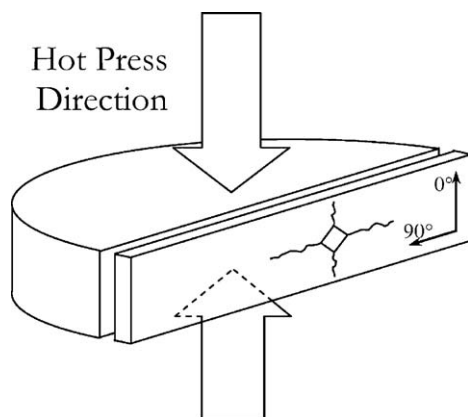*E-mail address:* dr@andrewcarman.com (A. Carman).

Fig. 1. Orientation of analysis plane, with respect to the hot pressing direction.

2. Experimental

The starting powders Si_3N_4 (H.C. Stark, Grade M11), AlN (H.C. Stark, Grade C), Al_2O_3 (Ajax Labchem) and Sm_2O_3 (ChemPur 99.9%) were measured out to give a composition of $Sm_{0.4}Si_{9.6}Al_{2.4}O_{1.2}N_{14.8}$, taking into account the surface oxides on the Si_3N_4 and AlN powders. The powders were milled using Si_3N_4 balls in isopropanol for 24 h and then dried. A hydraulic uniaxial press was used to make 1 in. pellets, which were then cold isostatically pressed at 200 MPa.

The samples were sintered by hot pressing at 1800 °C for 2 h under a load of 25 MPa, using a graphite die coated with BN for lubrication. The as-sintered material was heat treated at 1450 °C for 384 h in an alumina tube furnace under a high-purity nitrogen atmosphere, so as to promote the forward $\alpha' \to \beta'$ transformation. Such a long heat treatment time was necessary due to the very slow $\alpha' \to \beta'$ transformation rate in the Sm-sialon at the heat treatment temperature. The heat treated material was then re-sintered at 1800 °C for 2 h in a resistance graphite furnace under a high-purity nitrogen atmosphere, to promote the reverse $\beta' \to \alpha'$ transformation.

The surface layer (1.5–2 mm) was removed from the sample and the pellet was cut in half and a slice was cut off, as illustrated in Fig. 1. The samples were then polished to a mirror finish on a Struers RotoPol automatic polisher. Phase identification was carried out by X-ray diffraction (XRD) using a Phillips diffractometer with a Ni-filtered Cu K_α radiation source, which was performed on both the top and side surfaces (as defined in Fig. 1) so as to obtain spectra perpendicular and parallel (respectively) to the hot pressing direction. A small amount of each sample was crushed and ground to a fine powder using a boron carbide mortar and pestle, before being mixed with a silicon reference powder. XRD was then used to determine the lattice parameters of the α' phase, using regression analysis, as well as quantitatively determining the β' content, $\beta'/(\alpha' + \beta')$, as described by Gazzara and Messier.[9] The lattice parameters were then used to calculate the solid solution parameters (m and n) of the α-sialon phase ($Sm_{m/3}Si_{12-(m+n)}Al_{m+n}O_nN_{16-n}$) using[10]:

$$a\,(\text{Å}) = 7.752 + 0.036m + 0.02n \qquad (1)$$
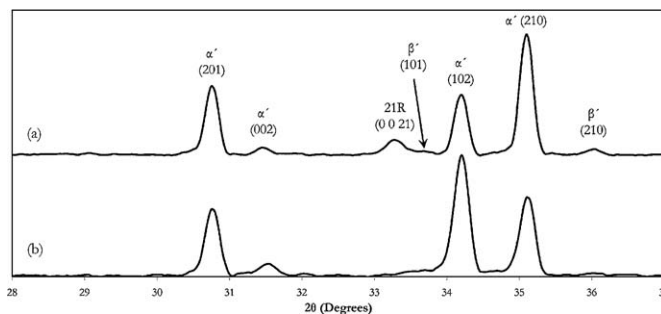
$$c\,(\text{Å}) = 5.620 + 0.031m + 0.04n \qquad (2)$$

Fig. 2. XRD spectra of as-sintered Sm-sialon (a) perpendicular and (b) parallel to the hot pressing direction.

After application of a carbon coating, microstructural analysis was performed on a Philips XL30 Scanning Electron Microscope (SEM) using back-scattered electron imaging. Distribution of the AlN polytypoid phase was determined by X-ray mapping (XRM) on a JEOL JSM 840A fitted with an Oxford EDXS detector. Image analysis of SEM micrographs and X-ray maps were then used to determine the volume fractions of the secondary phases present in the samples. A carbon coating was also applied to selected Transmission Electron Microscope (TEM) foils prepared using a low-energy PIPS Ar-ion mill, and the microstructures were studied in a Phillips CM20 TEM, operating at 200 kV.

The density was determined using Archimedes' principle, using water as the buoyant medium. A sintered pellet was cut into four wedges. All of the wedges were subjected to all heat treatments at the same time. The surfaces were removed from all four wedges after each heat treatment stage so as to remove any surface effects, and the density of each wedge was measured to give an average value.

The Vickers hardness and fracture toughness of the samples were measured by indentation using a Vickers diamond indenter under a load of 10 kg. The hardness and toughness were determined using the method of Anstis et al.[11]

3. Results and discussion

3.1. As-sintered material

The XRD spectra for the as-sintered Sm-sialon on both the top surface and the side face are shown in Fig. 2. The phases present in the sample are α', β' and the AlN polytypoid 21R, with α' as the majority phase, as previously reported.[12] A comparison of the XRD spectra for the orthogonal orientations in Fig. 2 indicates that the hot pressed material is preferentially oriented, as evidenced by the different relative intensities for the (2 1 0) and (1 0 2) reflections of the α' phase between the two spectra. The (2 1 0) reflection, which arises from a plane parallel to the c-axis of the unit cell, is much stronger in the plane perpendicular to the hot pressing direction than it is in the plane parallel to the hot pressing direction, whereas the (1 0 2) reflection, which diffracts from a plane that intersects the c-axis of the unit cell, shows the converse behaviour. Thus, the c-axis of the α' unit cell preferentially lies within the plane normal to the hot pressing direction.
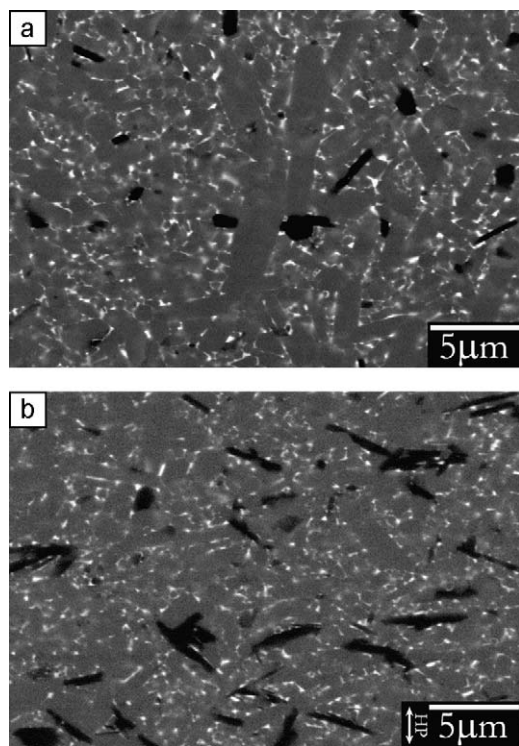
Fig. 3. SEM images of as-sintered Sm-sialon (a) perpendicular and (b) parallel to the hot pressing direction (indicated in (b)).

Table 1
Volume fractions (vol%) of phases present in as-sintered, heat treated and re-sintered samples.

	$\beta'/(\alpha' + \beta')$	α'	β'	21R	Nd-rich[a]
As-sintered	2	90	2	5	3
Heat treated	46	42	34	12	12
Re-sintered	6	83	6	7	4

[a] Nd-rich refers to grain boundary glass in as-sintered and re-sintered samples, or M'_{SS} in heat treated sample.

result in a crystallographic texture with the same preferential orientation.

As mentioned above, the β' and 21R phases appear as dark grains as neither phase contains samarium. Both phases also adopt elongated morphologies, so that identification by morphology is unreliable, particularly when heat treatment leads to phase transformations and grains coalesce and impinge on one another. However, it has been shown that 21R (SiAl$_6$O$_2$N$_6$) has a much higher aluminium content than β-sialon (Si$_{6-z}$Al$_z$O$_z$N$_{8-z}$), and elemental X-ray mapping of aluminium may be used to differentiate between the two phases.[14] Fig. 4 shows a back-scattered electron image of the as-sintered Sm-sialon, with the corresponding aluminium X-ray map. The β' and 21R are clearly distinguishable by comparing the two images, and noting the bright contrast in the X-ray map in Fig. 4(b) that coincides with dark grains in the back-scattered SEM image in Fig. 4(a). Using this method to distinguish between β' and 21R, semi-quantitative image analysis could then be applied to all of the phases present in the microstructure: α', β', 21R and the grain boundary phase. The results of the image analysis are provided in Table 1.

The TEM micrographs of the as-sintered material are provided in Fig. 5. The microstructure in Fig. 5(a) shows relatively defect free grains, while the high magnification images of the grain boundary junctions in Fig. 5(b) highlight the excellent wetting conditions of the liquid phase during sintering. The sharp, low-angle corners are clearly shown, with fine intergranular films in between adjacent grains.

3.2. Heat treated material

The hot pressed material was subjected to a post-sintering heat treatment at 1450 °C for 384 h, which resulted in the $\alpha' \rightarrow \beta'$

SEM was performed on both the top surface and side face of the as-sintered sample, as seen in Fig. 3. The white phase is the Sm-rich grain boundary glass, the grey phase is α', and the dark grains are either β' or 21R (as neither phase contains the rare-earth element). Both micrographs show a homogeneous microstructure with a fine, uniformly distributed grain boundary glass, and confirm that α' is the majority phase. Fig. 3 indicates that many α' grains have adopted an elongated morphology, and the side face in Fig. 3(b) illustrates the preferential orientation of the microstructure normal to the hot pressing direction, as evidenced by the prevalence of grains oriented along or close to the horizontal direction. Thus, the crystallographic texture identified by XRD coincides with the microstructural texture highlighted by SEM. This is not surprising, as the preferred grain growth direction for the α' phase is along the c-axis.[13] Therefore, the rotation of elongated α-sialon grains to preferentially lie normal to the hot pressing direction will
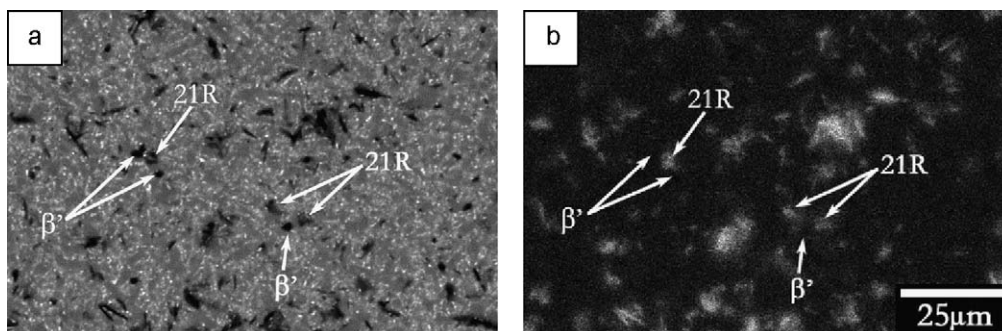

Fig. 4. (a) Back-scattered electron image of top surface of as-sintered Sm-sialon and (b) accompanying aluminium X-ray map.
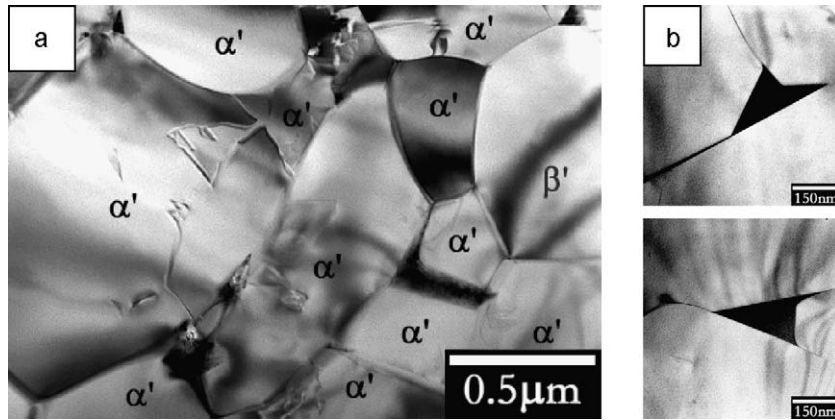
Fig. 5. Bright field TEM images of (a) microstructure and (b) grain boundary junctions in as-sintered Sm-sialon.

transformation, as seen from the significant increase in β′ in Fig. 6. The XRD spectra in Fig. 6 clearly show a decrease in α′, an increase in β′ and an increase in the melilite solid solution, M'_{SS}, indicating the α′ → β′ transformation with a corresponding formation of M'_{SS}. Of particular interest is the relative intensities of the XRD peaks in both the α′ and β′ phases, which indicate that the preferential orientation observed in the as-sintered sample was maintained during transformation. The (2 1 0) peaks of both sialon phases are stronger in the plane perpendicular to the hot pressing direction than in the pane parallel to the hot pressing direction. Although the ratios of the peaks suggest that the preferential orientation is not as strong as in the as-sintered sample, the α′ and β′ phases are clearly preferentially oriented. Of particular note is the presence of a preferential orientation in the β′ phase. The maintenance of a preferential orientation during the α′ → β′ transformation under pressureless conditions suggests a crystallographic relationship between the transformation phases. This phenomenon has been observed in Nd-sialons which contained 11 vol% β′ prior to heat treatment.[3] However, the as-sintered material in the current study only contained 2 vol% β′, dramatically reducing the number of heterogeneous β′–β′ nucleation sites. Thus, a crystallographic relationship is confirmed between the parent α′ phase and the transformed β′ phase.

The microstructure of the heat treated sample in Fig. 7 confirms the transformation of α′ to β′, as seen by the dramatic increase in the dark phase. The micrographs also illustrate the grain boundary migration and agglomeration seen during the

early stages of heat treatment,[7,15] resulting in large areas poor in M'_{SS} (Fig. 7(a)) and areas rich in M'_{SS} (Fig. 7(b)). It can be seen that the morphology of the β′ grains in the heat treated sample appears to be bimodal. Fig. 7 exhibits a large number of small, slightly elongated β′ grains and a small number of large, very elongated β′ grains, with higher aspect ratios than the α′ grains in the as-sintered sample. The small, less elongated β′ grains may be the result of large elongated β′ grains intersecting the viewing plane at an angle. However, given the presence of the two-dimensional preferential orientation described above, the number of grains intersecting the top surface at high angles is greatly reduced from that in an untextured sample. Thus, the bimodal grain morphology suggests that the large, very elongated β′ grains are the result of epitaxial growth on pre-existing

Fig. 7. SEM images of Sm-sialon heat treated at 1450 °C for 384 h (a) M'_{SS}-poor region and (b) M'_{SS}-rich region.
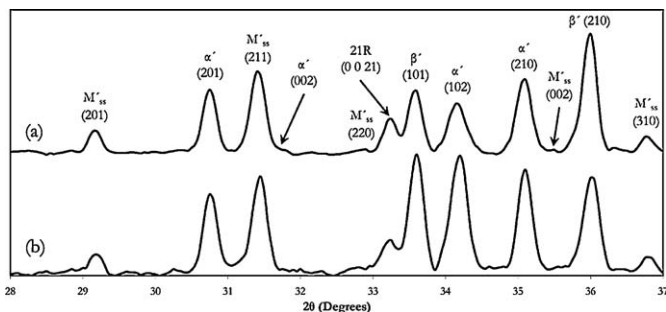

Fig. 6. XRD spectra of Sm-sialon heat treated at 1450 °C for 384 h (a) perpendicular and (b) parallel to the hot pressing direction.
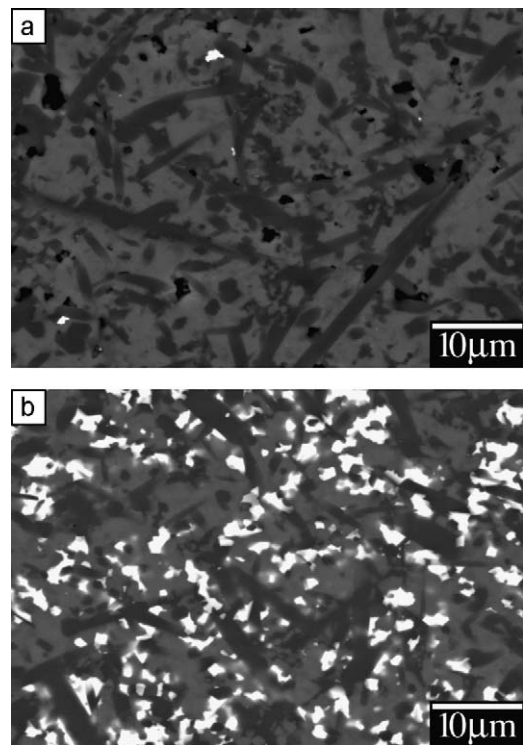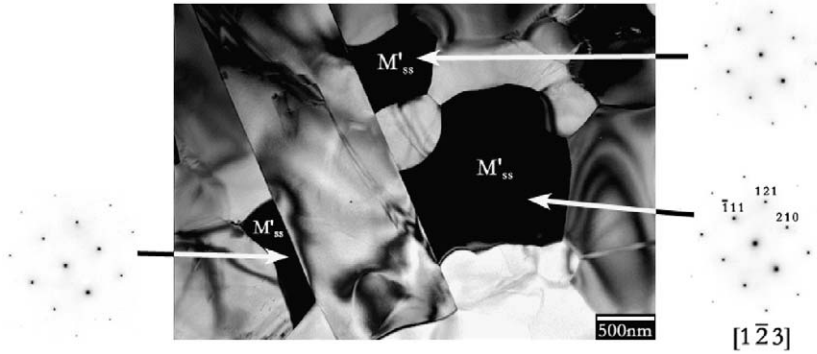
Fig. 8. TEM bright field image of M'_{SS} "grains" in Sm-sialon heat treated at 1450 °C for 384 h, along [1 $\bar{2}$ 3] zone axis and corresponding diffraction patterns.

β' (from the as-sintered microstructure), while the smaller β' grains result from heterogeneous nucleation on the parent α' phase throughout the microstructure and subsequent growth during heat treatment.

In a conventional glass-ceramic process, devitrification of a glass usually takes place at a temperature at which the glass remains in a solid state. The high heat treatment temperature of 1450 °C used in this study decreases the viscosity of the grain boundary glass and facilitates grain boundary glass migration and agglomeration, in addition to devitrification. The M'_{SS} agglomerates shown in Fig. 7 were formed by the devitrification of the grain boundary glass and de-wetting of the grain boundary phase from the sialon grains. This de-wetting and migration, and subsequent agglomeration, act to minimise the surface energy of the grain boundary glass and results in an inhomogeneous distribution of the M'_{SS} phase, as seen previously in this composition.[16] However, particle rearrangement was limited during heat treatment, thereby resulting in the formation of voids at the grain boundaries, particularly in the M'_{SS}-poor regions from which the grain boundary glass migrated.

Crystallographic analysis of the M'_{SS} agglomerates indicated that the individual grains seen in the SEM images were, in fact, part of a three-dimensional network of melilite that formed around a large number of grains. Fig. 8 shows three apparently separated M'_{SS} "grains" that exhibited the same diffraction pattern along parallel zone axes, indicated by the surrounding diffraction patterns. Many other examples of crystallographically aligned "grains" of M'_{SS} in close proximity to each other were observed throughout the sample. Thus, the cross-sections of the microstructures seen in the SEM and TEM images are intersections of melilite networks that form what appears as isolated grains. This phenomenon has been previously observed in the Y–Si–Al–O–N[17] and Mg–Si–Al–O–N[18] systems, where the devitrification products formed large crystal networks. The current observations of large areas of M'_{SS}-rich and M'_{SS}-poor regions in the sample are consistent with the previous work that identified a low nucleation density. However, the reason for such a low nucleation density, despite a large β'-glass interfacial area that should act as a heterogeneous nucleation catalyst, remains unclear. Lewis et al.[17] suggested nucleation on pores, however, the hot-pressed samples showed no observable porosity, despite extensive observation by electron microscopy. Thus, the sec-

ondary nucleation mechanism, the competition between direct nucleation of the melilite and the indirect nucleation through an aluminate,[16] seems more likely.

During post-sintering heat treatment, separate M'_{SS} grains form simultaneously and grow around sialon grains. After sufficient agglomeration and growth, the M'_{SS} grains form small networks around sialon grains that coalesce to form a larger interconnected network of the melilite phase. Thus, the large interconnected network is made up of smaller networks of melilite, each of which has its own crystallographic orientation. These smaller networks of uniform crystallographic orientation have sizes given by the nucleation distribution of the M'_{SS} phase.

Further analysis of the heat treated microstructure by TEM confirms an increased β' content and the network of melilite phase, as shown in Fig. 9. Almost all of the β' grains contain a significant number of dislocations. From the β' contents before and after heat treatment, over 95% of the β' in the heat treated sample is transformed β'. Therefore, it is clear that the dislocations arise from transformation. This has been proposed before for Sm-sialons.[19–21] However, in the previous studies, the dislocations were associated with stabilising cation-rich nano-inclusions. No nano-inclusions are evident in Fig. 9, nor were
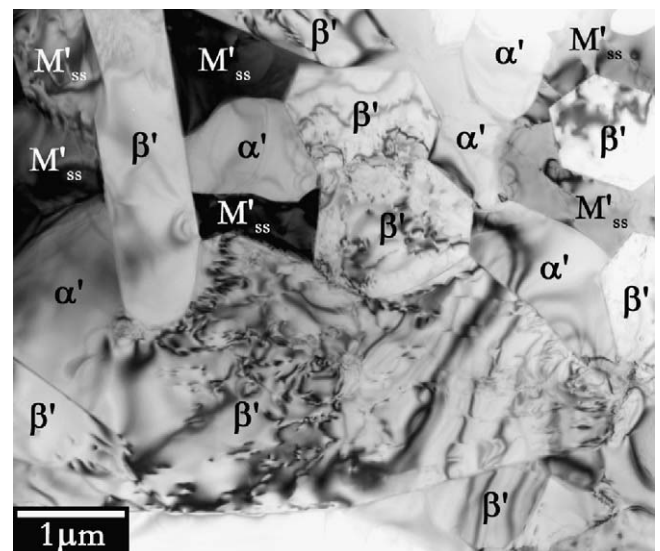

Fig. 9. TEM bright field image of Sm-sialon heat treated at 1450 °C for 384 h.
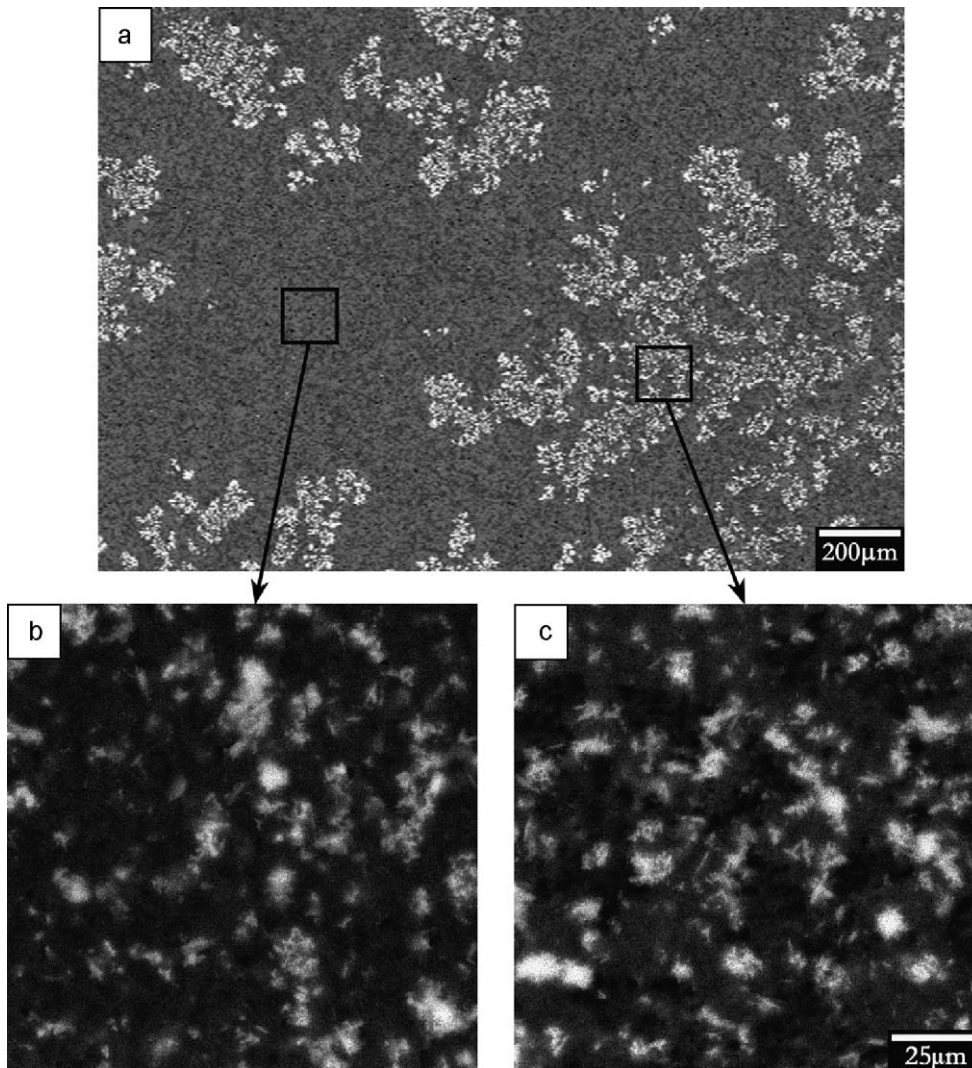
Fig. 10. (a) SEM image of top surface of sample heat treated at 1450 °C for 384 h and accompanying aluminium X-ray maps of (b) M'_{SS}-poor region and (c) M'_{SS}-rich region.

any observed in a more detailed TEM analysis of the sample. This is most likely due to the slow transformation rate in this investigation, which allowed adequate time for diffusion of the elements along the dislocations to the grain boundary, thereby removing the inclusions.

The inhomogeneity of the M'_{SS} phase suggests the possibility that other phases may differ in volume fraction between M'_{SS}-rich and M'_{SS}-poor regions. This is demonstrated in Fig. 10, where aluminium X-ray maps of M'_{SS}-rich and M'_{SS}-poor regions appear to indicate a different amount of 21R between the two areas. Image analysis of the corresponding back-scattered electron micrographs found that the phase assemblages in the M'_{SS}-rich and M'_{SS}-poor regions are 59% α'–10% β'–16% 21R–15% M'_{SS} and 54% α'–33% β'–13% 21R, respectively. Thus, the α':β' ratio is much lower in the M'_{SS}-poor area, where there is very little grain boundary phase remaining. As the $\alpha' \rightarrow \beta'$ transformation involves the rejection of the stabilising cation from the decomposing α' phase, the presence of a high concentration of the cation (such as in the M'_{SS}-rich regions) will locally decrease the driving force for transformation. Con-

versely, the migration of the grain boundary liquid away from the M'_{SS}-poor regions will promote further diffusion of samarium from the α' phase as it transforms to β', thereby increasing the degree of $\alpha' \rightarrow \beta'$ transformation in that region. This is consistent with earlier work, where it was observed that the β' content was suppressed in the immediate vicinity of the M'_{SS} agglomerates.[22]

If the SEM and XRM image analyses are done over a number of regions, an average may be determined, which is given in Table 1. These results show that, in addition to the formation and increase in M'_{SS}, the volume fraction of the 21R polytypoid increases during heat treatment. Thus, the $\alpha' \rightarrow \beta'$ transformation that occurs during post-sintering heat treatment is accompanied by the formation of the melilite phase as well as the AlN polytypoid 21R, giving a transformation reaction of:

$$\alpha' + \text{liquid} \rightarrow \beta' + M'_{SS} + 21R \qquad (3)$$

This reaction involves the dissolution of α' into the liquid phase, from which the β' is precipitated. The excess samarium and aluminium in the liquid phase resulting from the com-
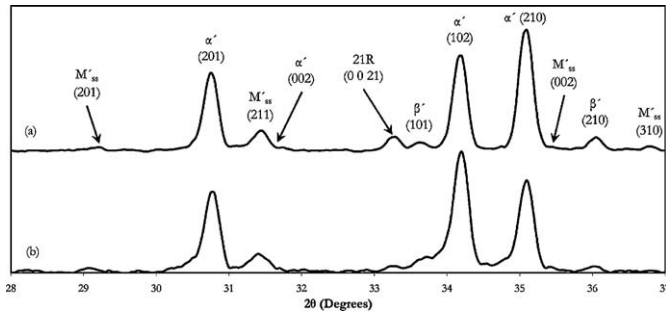
Fig. 11. XRD spectra of Sm-sialon re-sintered at 1800 °C for 2 h (a) perpendicular and (b) parallel to the hot pressing direction.

Fig. 12. SEM image of top surface Sm-sialon re-sintered at 1800 °C for 2 h.

positional difference between the α' and β' phases are then incorporated into the M'_{SS} and 21R, respectively. It is likely that the significant compositional change in the residual liquid after the solution-precipitation process makes the liquid phase unstable and crystallisation occurs at, or immediately below, the heat treatment temperature. The α' phase was initially formed during hot pressing at 1800 °C. Its dissolution into the grain boundary liquid at a temperature much lower than the initial sintering temperature suggests that the α' composition is metastable and will decompose when a liquid phase is present, allowing adequate diffusion.

3.3. Re-sintered material

The sample that was heat treated at 1450 °C for 384 h was subsequently re-sintered at 1800 °C for 2 h. The XRD spectra of the top surface and side face are shown in Fig. 11 indicating a significant decrease in the β' content compared to that in the sample heat treated at 1450 °C. Quantitative XRD analysis found the $\beta'/(\alpha' + \beta')$ volume fraction to be 6 vol%, which is close to that of the as-sintered material (2 vol%). In fact, the α' and β' peaks in the XRD spectra in Fig. 11 are very similar in relative intensities to those in the as-sintered sample in Fig. 2. This clearly confirms the reversibility of the $\alpha' \leftrightarrow \beta'$ transformation already reported.[1,2] In addition, the M'_{SS} peaks in the XRD spectra have almost disappeared. This is to be expected, as the re-sintering temperature of 1800 °C is above the melting temperature of Sm-M'_{SS}.[12] Thus, it appears that a majority of the M'_{SS} phase melted during re-sintering, leaving only a small amount of residual melilite in the re-sintered sample.

Again, a comparison of the XRD spectra for the planes perpendicular and parallel to the hot pressing direction indicates a preferential orientation of the sialon phases. The relative intensity of the (2 1 0) reflection is stronger in the top surface than in the side face for both of the α' and β' phases. Thus, the preferential orientation of the c-axis normal to the initial hot pressing direction, which has been observed in all previous samples, has been maintained during the reverse $\beta' \rightarrow \alpha'$ transformation. The continued presence of a preferential orientation in the sialon samples during pressureless re-sintering confirms that there is a crystallographic relationship between the transformation phases in both the forward and reverse routes of the reversible $\alpha' \leftrightarrow \beta'$ transformation.
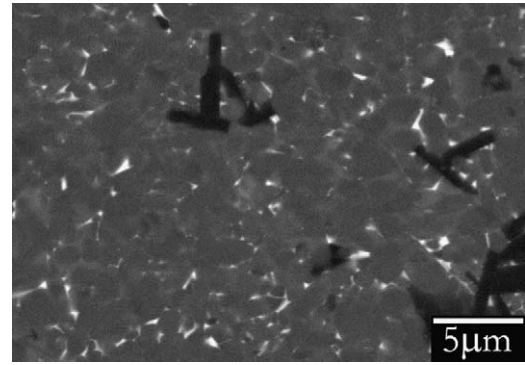
A SEM micrograph of the re-sintered sample, shown in Fig. 12, confirms α' as the majority phase in the re-sintered microstructure, verifying the reverse $\beta' \rightarrow \alpha'$ transformation during re-sintering. The re-sintered microstructure is similar to that of the as-sintered sample in Fig. 3, except for a certain degree of grain growth. This grain growth is a result of the sample having undergone significant heating – 2 h at 1800 °C during the initial sintering, 384 h at 1450 °C during post-sintering heat treatment and another 2 h at 1800 °C during re-sintering. The grain boundary phase is, again, uniformly distributed throughout the microstructure. However, the grain boundary junctions are coarser as a result of the sialon grain growth. The uniformity of the grain boundary phase, and the presence of sharp corners on the grain boundary junctions, indicates that the liquid phase readily re-wetted the grain boundaries at the re-sintering temperature. However, the fine, intergranular layers are not as prevalent in the re-sintered sample as in the as-sintered material.

A comparison of the grain boundary phases between the heat treated microstructure and the re-sintered microstructure indicates that most of the agglomerated M'_{SS} in the heat treated sample has, indeed, melted at the re-sintering temperature. Image analysis determined that the M'_{SS} volume fraction in the heat treated sample was 12 vol% and the volume fraction of grain boundary phase in the re-sintered sample was 4 vol%. Therefore, not only did the M'_{SS} melt during re-sintering, but the resulting liquid was also consumed during the reverse $\beta' \rightarrow \alpha'$ transformation. In fact, the grain boundary glass content has almost been reduced to the amount observed in the as-sintered sample (3 vol%).

The extent of the re-wetting of the liquid phase on the sialon grains during re-sintering at 1800 °C is illustrated in Fig. 13(a). The two grain boundary junctions (dark) in the image were confirmed to be glass by the diffuse diffraction beam (inset), and both junctions exhibit very sharp, low angle corners, indicating good wetting at the re-sintering temperature. However, the XRD spectra indicated that the M'_{SS} was not completely melted, and this is confirmed in Fig. 13(b). The small triple-point junction contains the crystalline M'_{SS} phase, as evidenced by the diffraction pattern, in addition to glass. The morphologies of the glass and M'_{SS} phases in the triple point junction in Fig. 13(b) indicate that the interface between the phases is a convex melt front propagating through the residual M'_{SS} grain.
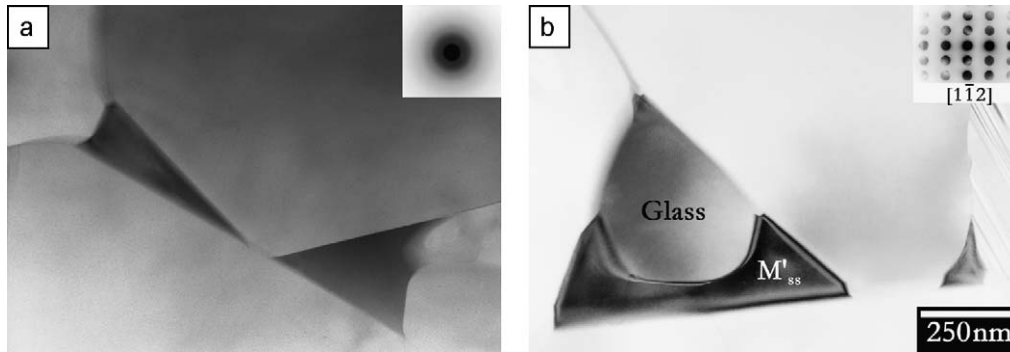
Fig. 13. TEM bright field image of grain boundary junctions containing (a) amorphous glass (with insert of diffuse diffraction beam) and (b) glass and melilite (with inset of M'_{SS} Convergent Beam Electron Diffraction (CBED) pattern along [1 $\bar{1}$ 2] zone) in Sm-sialon re-sintered at 1800 °C for 2 h.

The aluminium X-ray map of the re-sintered sample is presented in Fig. 14, which clearly shows a decrease in 21R compared to the heat treated sample in Fig. 10. Image analysis confirmed this, as shown by the decreased content of the 21R phase in Table 1. This decrease indicates that the AlN polytypoid was consumed during the reverse $\beta' \rightarrow \alpha'$ transformation. Thus, the reverse $\beta' \rightarrow \alpha'$ transformation that occurred at 1800 °C was accompanied by the simultaneous decrease of the volume fractions of the M'_{SS} and 21R phases. This confirms the full reversible transformation reaction as being:

$$\alpha' + liquid \leftrightarrow \beta' + M'_{SS} + 21R \qquad (4)$$

During the reverse transformation of Eq. (4), most of the M'_{SS} melts and the resulting liquid re-wets the sialon grains, acting as a source for the stabilising cation. The samarium diffuses into the α' grains to stabilise the crystal structure, thereby decreasing the amount of liquid phase. This is confirmed by image analysis, which found that the final volume fraction of the grain boundary phase was much less than the amount of liquid that would have resulted from the melting of the M'_{SS} phase. Thus, the liquid was consumed during reverse $\beta' \rightarrow \alpha'$ transformation. Agglomeration of the M'_{SS} phase during heat treatment at 1450 °C has been reported for the Sm-sialon system.[22] However, no work has yet been published on the effect of subsequent high-temperature heat treatments on the secondary phase.
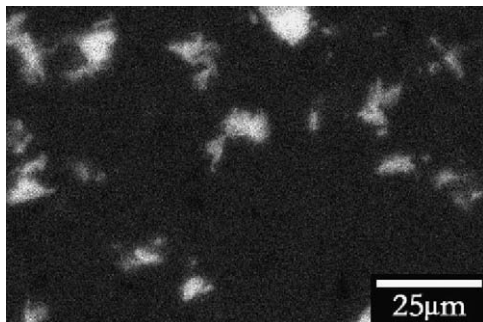
3.4. Transformation cycle

The lattice parameters and, from these, the solid solubility parameters, of the α' phase were determined from precision X-ray diffraction. The results are given in Table 2, showing a non-reversible trend in both lattice parameters and composition, despite the thermodynamic reversal of the $\alpha' \leftrightarrow \beta'$ transformation. This is in contrast with the reversibility of Nd-sialons, where the lattice parameters and solid solubilities were found to be generally reversible during transformation cycling.[3] This is most likely due to the non-equilibrium condition used during re-sintering, particularly as the re-sintering time was decreased. Although the original hot pressing schedule and the re-sintering schedule used the same time and temperature, the starting condition (prior to heating) was very different. That is, the as-sintered sample was produced by heating the raw powder mix, while the re-sintered sample resulted from heating a pre-sintered, densified sample. As a result, it may have been that an equilibrium distribution of elements (particularly for the heavy rare-earth element) was not established and the compositions in the re-sintered sample were affected.

The density of the Sm-sialon was determined after hot-pressing, heat treatment and re-sintering, and the results are shown in Fig. 15(a). It can be seen that the density decreases with heat treatment at 1450 °C, accompanying the $\alpha' \rightarrow \beta'$ transformation. After re-sintering at 1800 °C for 2 h, the density decreases further during the reverse $\beta' \rightarrow \alpha'$ transformation. It is believed that the changes in density are predominantly due to the development of porosity in the bulk of the samples after the heat treatment stages. Porosity was observed in the micrographs of the samples and was measured by image analysis. The results are given in Fig. 15(b). It is clear that the increase in poros-

Fig. 14. Aluminium X-ray map of Sm-sialon re-sintered at 1800 °C for 2 h.

Table 2
Lattice parameters and corresponding solid solution parameters of α-sialon during $\alpha' \leftrightarrow \beta'$ transformation cycle.

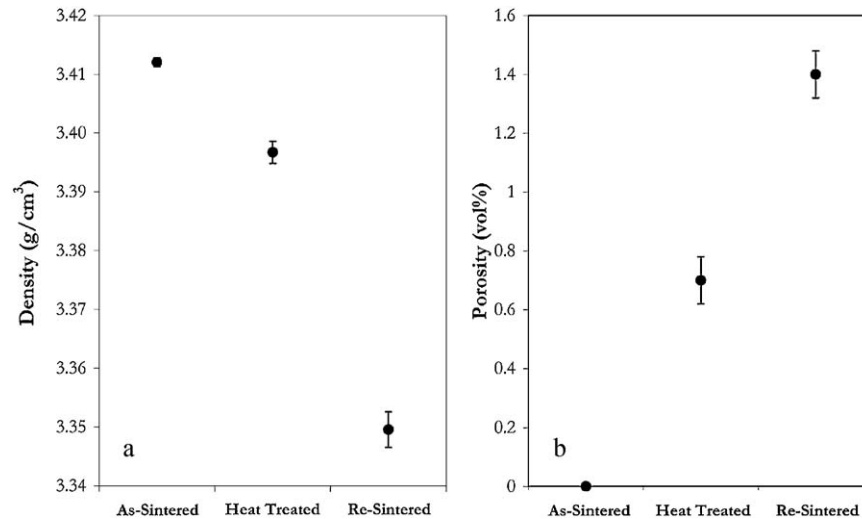|	a (Å)	c (Å)	m	n
As-sintered	7.804 ± 0.003	5.691 ± 0.005	0.80	1.15
Heat treated	7.812 ± 0.001	5.692 ± 0.004	1.19	0.88
Re-sintered	7.815 ± 0.001	5.693 ± 0.002	1.29	0.84

Fig. 15. (a) Density and (b) bulk porosity of the as-sintered, heat treated and re-sintered Sm-sialon samples.

ity after heat treatment and re-sintering correlates well with the decrease in density.

These results agree with the changes in density of certain compositions (using Nd, Dy and Yb sialons) after heat treatment and re-sintering, although no explanation was offered for that behaviour.[2] However, the changes in density in the current study are very different to those observed for a Nd-sialon that had an equivalent molar composition, where the density fluctuated reliably with transformation cycling.[3] This was due to the considerable degree of agglomeration of the M'_{SS} phase in the Sm-sialon system during heat treatment at $1450\,^{\circ}C$. As can be seen in Fig. 16(a), the migration of the grain boundary phase resulted in porosity (black) in the M'_{SS}-poor regions. The M'_{SS}-rich areas, on the other hand, show no porosity, as the three-dimensional network of agglomerated M'_{SS} filled any pores that may have developed during heat treatment.

Subsequent re-sintering at $1800\,^{\circ}C$, however, resulted in even more porosity being formed, as indicated in Fig. 15(b) and seen from the microstructure in Fig. 16(b). A comparison of the distribution of M'_{SS} in the heat treated sample and the distribution of porosity in the re-sintered sample shows a degree of similarity in scale and inhomogeneity. Thus, it appears that the increase in porosity after re-sintering at $1800\,^{\circ}C$ was primarily a result of the melting of the agglomerated melilite and the re-distribution

of the resulting liquid phase throughout the microstructure. The pores that formed when the coarse agglomerated melilite network was melted were large and required a significant degree of particle re-arrangement to remove the porosity. There was no significant solution-precipitation of sialon phases involved during the re-sintering and thus the porosity could not be removed through sialon grain re-arrangement.

In contrast to the α-sialon lattice parameters and sample density, the mechanical properties appeared to be reversible, as can be seen from the hardness and toughness results in Table 3. All measurement in Table 3 almost returned to the as-sintered value after re-sintering. Thus, the reversibility of the α′ ↔ β′ transformation resulted in the reversibility of the mechanical properties, despite the further deteriorating physical properties (density and porosity). Therefore, it appears that the dominant factor in determining the mechanical properties of the sialon ceramic is the α′:β′ ratio, while other factors, such as the density and porosity, are less important. This has been established for sialon ceramics through compositional design[23] or post-sintering heat treatment.[3]

The mechanical properties measured on the side face demonstrated property anisotropy resulting from the texture introduced by hot pressing as a function of the α′ ↔ β′ transformation cycle. The hardness does not exhibit any noticeable anisotropy.

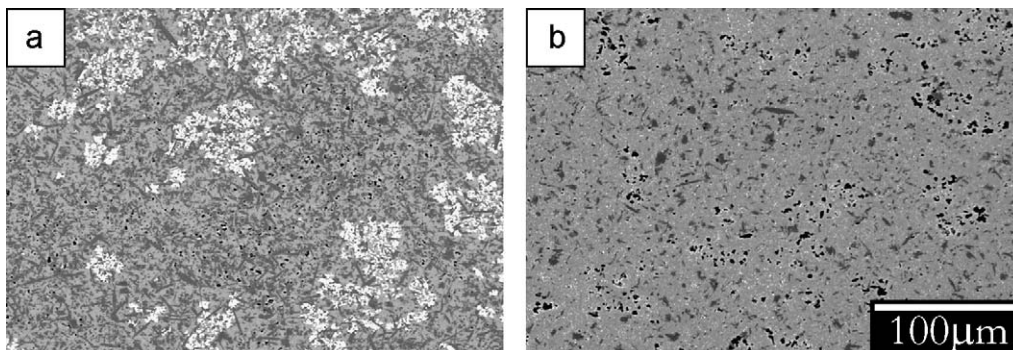Fig. 16. SEM images of Sm-sialon (a) heat treated at $1450\,^{\circ}C$ for $384\,h$ and (b) re-sintered at $1800\,^{\circ}C$ for $2\,h$, highlighting bulk porosity (black).

Table 3
Hardness and toughness values during $\alpha' \leftrightarrow \beta'$ transformation cycle.

	Top surface		Side face			
			Perpendicular to HP		Parallel to HP	
	H_v (GPa)	K_C (MPa m$^{1/2}$)	H_v (GPa)	K_C (MPa m$^{1/2}$)	H_v (GPa)	K_C (MPa m$^{1/2}$)
As-sintered	20.6 ± 0.7	4.0 ± 0.4	21.0 ± 0.5	3.4 ± 02.	21.7 ± 0.5	4.3 ± 0.2
Heat treated	18.1 ± 0.8	4.8 ± 0.4	17.7 ± 0.6	4.2 ± 0.3	17.6 ± 0.4	5.4 ± 0.5
Re-sintered	19.6 ± 0.6	4.0 ± 0.3	19.6 ± 0.9	3.7 ± 0.2	19.0 ± 0.8	4.5 ± 0.4

However, the toughness shows a much stronger dependence on the orientation, with the toughness being greater along the hot pressing direction. This is a result of the preferentially oriented elongated sialon grains, which will tend to increase the crack path parallel to the hot pressing direction, thereby increasing the energy required to crack the material and increase its toughness. This anisotropy is also maintained during the transformation cycle.

Thus, multiple heat treatments of a Sm-sialon at 1450 °C and then at 1800 °C has clearly established the reversibility of the $\alpha' \leftrightarrow \beta'$ transformation in Sm-sialon ceramics, thermodynamically and, to a certain extent, microstructurally. Other features, such as the α-sialon composition and the density, were not reversible. As the major contributions to the hardness and toughness are the α' and β' contents and the microstructure, the mechanical properties show a similar reversibility to the $\alpha' \leftrightarrow \beta'$ transformation and the microstructure. Therefore, any changes in the Sm-sialon material associated with use of the material at elevated temperatures (1000–1500 °C) may be partially recovered by re-sintering at 1800 °C.

4. Conclusions

(1) A texture was introduced into Sm-sialon by hot pressing, such that the *c*-axes of the α' and β' phases lay preferentially in the plane perpendicular to the hot pressing direction.

(2) Post-sintering heat treatment at 1450 °C promoted the forward $\alpha' \to \beta'$ transformation, accompanied by an increase in the M'_{SS} and 21R contents. Subsequent re-sintering at 1800 °C resulted in the reverse $\beta' \to \alpha'$ transformation, with an accompanying reduction of the secondary phases, M'_{SS} and 21R, such that the full transformation reaction should be:

$$\alpha' + \text{liquid} \leftrightarrow \beta' + M'_{SS} + 21R$$
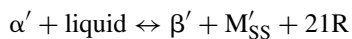
(3) The preferential orientation introduced by hot pressing was found to be preserved during both the $\alpha' \to \beta'$ and $\beta' \to \alpha'$ stages of the transformation cycle, indicating that there is a crystallographic relationship between the transformation phases during both the forward and reverse routes of the $\alpha' \leftrightarrow \beta'$ transformation.

(4) The Sm–Si–Al–O–N grain boundary liquid underwent significant migration and agglomeration during heat treatment at 1450 °C, forming inhomogeneous three-dimensional networks of melilite throughout the microstructure.

(5) The migration of the grain boundary liquid resulted in a decreased rate of $\alpha' \to \beta'$ transformation in the regions of M'_{SS} agglomeration, due to enrichment of the stabilising cation which increased the energy barrier for transformation.

(6) The microstructure and mechanical properties were found to be mostly reversible, while the α' lattice parameters and bulk density were not reversible at all.

References

1. Mandal H, Thompson DP, Ekström T. Reversible $\alpha' \leftrightarrow \beta'$ sialon transformation in heat-treated sialon ceramics. *J Eur Ceram Soc* 1993;**12**(6):421–9.
2. Liu Q, Gao L, Yan DS, Thompson DP. Thermal stability and mechanical performance of multiply heat-treated α-sialon ceramics densified with rare earth oxides. *J Mater Sci* 2000;**35**(9):2229–33.
3. Carman A, Pereloma E, Cheng Y-B. Reversible $\alpha' \leftrightarrow \beta'$ transformation in preferentially oriented sialon ceramics. *J Eur Ceram Soc* 2006;**26**(8):1337–49.
4. Mandal H, Camuşcu N, Thompson DP. Comparison of the effectiveness of rare-earth sintering additives on the high-temperature stability of α-sialon ceramics. *J Mater Sci* 1995;**30**(23):5901–9.
5. Camuşcu N, Thompson DP, Mandal H. Effect of starting composition, type of rare earth sintering additive and amount of liquid phase on $\alpha \leftrightarrow \beta$ sialon transformation. *J Eur Ceram Soc* 1997;**17**(4):599–613.
6. Rosenflanz A, Chen I-W. Kinetics of phase transformations in SiAlON ceramics: I. Effects of cation size, composition and temperature. *J Eur Ceram Soc* 1999;**19**(13–14):2325–35.
7. Zhao R, Cheng Y-B. Phase transformations in Sm $(\alpha + \beta)$-SiAlON ceramics during post-sintering heat treatments. *J Eur Ceram Soc* 1995;**15**(12):1221–8.
8. Mandal H, Thompson DP. The driving force for $\alpha' \leftrightarrow \beta'$ transformation in rare earth α sialon ceramics. *Key Eng Mater* 1997;**132–136**:798–801.
9. Gazzara CP, Messier DR. Determination of phase content of Si$_3$N$_4$ by X-ray diffraction analysis. *Ceram Bull* 1977;**56**(9):777–80.
10. Shen Z, Nygren M. On the extension of the α-sialon phase area in yttrium and rare-earth doped systems. *J Eur Ceram Soc* 1997;**17**(13):1639–45.
11. Anstis GR, Chantikul P, Lawn BR, Marshall DB. A critical evaluation of indentation techniques for measuring fracture toughness: I. Direct crack measurements. *J Am Ceram Soc* 1981;**64**(9):533–8.
12. Cheng Y-B, Thompson DP. Preparation and grain boundary devitrification of samarium α-sialon ceramics. *J Eur Ceram Soc* 1994;**14**(1):13–21.
13. Zhao H, Swenser SP, Cheng Y-B. Elongated α-sialon grains in pressureless sintered sialon ceramics. *J Eur Ceram Soc* 1998;**18**(8):1053–7.
14. Zhao R, Swenser SP, Cheng Y-B. Formation of AlN-polytypoid phases during α-SiAlON decomposition. *J Am Ceram Soc* 1997;**80**(9):2459–63.
15. Ekström T, Falk LKL, Shen Z-J. Duplex α,β-sialon ceramics stabilized by dysprosium and samarium. *J Am Ceram Soc* 1997;**80**(2):301–2.
16. Carman A, Pereloma EV, Cheng Y-B. Grain boundary evolution in Sm- and Nd-sialons during post-sintering heat treatment. *J Aust Ceram Soc* 2009;**45**(1):27–34.

17. Lewis MH, Bhatti AR, Lumby RJ, North B. The microstructure of sintered Si–Al–O–N ceramics. *J Mater Sci* 1980;**15**(1):103–13.

18. Lewis MH, Bhatti AR, Lumby RJ, North B. Crystallization of Mg-containing phases in β′-Si–Al–O–N ceramics. *J Mater Sci* 1980;**15**(2):438–42.

19. Zhao R, Cheng Y-B. Decomposition of Sm α-SiAlON phases during post-sintering heat treatment. *J Eur Ceram Soc* 1996;**16**(9):1001–8.

20. Zhao R, Cheng Y-B, Drennan J. Microstructural features of the α to β-sialon phase transformation. *J Eur Ceram Soc* 1996;**16**(5):529–34.

21. Swenser SP, Pereloma EV, Cheng Y-B. Nano-inclusions associated with β-SiAlON grains in α–β SiAlON materials. *Key Eng Mater* 1997;**132–136**:1014–7.

22. Seeber AJ, Cheng Y-B, Harrowfield I. Phase and microstructural evolution during the heat treatment of Sm–Ca–α-sialon ceramics. *J Eur Ceram Soc* 2002;**22**(9):1609–20.

23. Zhang C, Sun WY, Yan DS. Optimizing mechanical properties and thermal stability of Ln-α-β-sialon by using duplex Ln elements (Dy and Sm). *J Eur Ceram Soc* 1999;**19**(1):33–9.